Reduced Order Models at work

Michel Bergmann, Thierry Colin, Angelo Iollo, Damiano Lombardi, Olivier Saut, Haysam Telib

Reduced Order Models at Work

Michel Bergmann, Thierry Colin, Angelo Iollo, Damiano Lombardi, Olivier Saut, Haysam Telib

Abstract We review a few applications of reduced-order modeling in aeronautics and medicine. The common idea is to determine an empirical approximation space for a model described by partial differential equations. The empirical approximation space is usually spanned by a small number of global modes. In case of periodic or mainly diffusive phenomena it is shown that this approach can lead to accurate fast simulations of complex problems. In other cases, models based on definition of transport modes significantly improve the accuracy of the reduced model.

1 Introduction

Progress in numerical simulation of partial differential equations (PDEs) allows accurate and reliable predictions of some complex phenomena in solid and fluid mechanics, solid state physics, geophysics, etc., at the price of significant code developments, difficult computational set ups and large high-performance computing infrastructures. Using reduced-order models (ROMs) one trades accuracy for speed

Michel Bergmann
Inria, F-33400 Talence, France, e-mail: michel.bergman@inria.fr

Thierry Colin
Université de Bordeaux and Inria, F-33400 Talence, France, e-mail: thierry.colin@inria.fr

Angelo Iollo
Université de Bordeaux and Inria, F-33400 Talence, France, e-mail: angelo.iollo@inria.fr

Damiano Lombardi
Inria, F-78153 Rocquencourt, France, e-mail: damiano.lombardi@inria.fr

Olivier Saut
CNRS and Inria, F-33400 Talence, France, e-mail: olivier.saut@inria.fr

Haysam Telib
Optimad Engineering, I-10143 Torino, Italy, e-mail: haysam.telib@optimad.it

and scalability, and counteracts the curse of dimension by significantly reducing the computational complexity. Thus ROMs represent an ideal building block of systems with real-time requirements, like interactive decision support systems that offer the possibility to explore various alternatives. In complex cases, the real-time requirements would not be met by standard numerical methods.

The construction of ROMs for design, optimization, control and data-driven systems is a non-trivial task and various alternative ways can be followed often without any guarantee that the ROM will effectively model the physical phenomenon in the application. Focusing for example on flows or environmental phenomena, different states can often be characterized by the presence or absence of qualitative flow features, by the structure of feature patterns and by the strength of such features. Proper orthogonal decomposition (POD) [9, 10] is a mean to extract such features from existing solution snapshots under the form of global modes. However, ROMs based on such POD modes are numerically unstable in unsteady, advection dominated models. Stabilization can be obtained by various ad hoc techniques (see [5, 1, 13, 2] for example), but a general framework to determine accurate and robust unsteady ROMs is still lacking. Still, ROMs can be useful to model far-field conditions coupled to a complete model, or to regularize the solution of an inverse problem. We give in the following two examples in these directions.

Another central issue for ROMs is the quality of the approximation obtained thanks to a reduced number of empirical modes. These modes are determined from a set of snapshots that are relative to a particular configuration: geometry, physical parameters, boundary conditions. When the configuration varies there is no guarantee that the reduced basis will adequately approximate the solution. On the other hand, if the snapshot set from which the basis is obtained includes a large number of different configurations, by construction the reduced basis will enjoy better approximation properties when the configuration varies. Given the computational costs relative to a systematic exploration of the configuration space, optimal sampling strategies must be introduced. In the following, we present one strategy based on an estimation of the approximation error of the reduced base.

Nevertheless, there is a fundamental difficulty in approximating with global (for example POD) modes the displacement of, say, a flow feature in time or across the parameter space. Global modes are not optimal for advection. In particular, POD modes reduce to Fourier modes for translation invariant signals. An alternative idea is to define advection modes as the solution of an optimal transportation problem. An application to interpolate the solution of a PDE system across the parameter space based on the definition of advection modes is presented in the following.

2 Systematic sampling for ROM

We have considered an oscillating NACA0012 airfoil in a compressible flow as in the CT1 test case from AGARD-R702 report. This case corresponds to a Mach 0.6 flow at infinity past an oscillating NACA0012 airfoil. In the following the compu-

tations are inviscid; in the actual experiments the Reynolds number is 4.8×10^6. The parameter space is two dimensional: the oscillating frequency varies between f^1 =30Hz and f^2 =70Hz (CT1 case: 50Hz) whereas the amplitude of the oscillation varies between α_0^1=1.6deg and α_0^2=3.6deg (CT1: 2.5deg) with an average pitch of α_m=3.0deg. We have implemented an algorithm to sample the parameter space in order to enrich the database of the POD basis functions. The objective of this procedure is to determine a set of POD modes that minimizes the approximation error across the parameter space $S = [\alpha_0^1, \alpha_0^2] \times [f^1, f^2]$.

The main idea is to build a recursive Voronoi diagram and the corresponding Delaunay triangulation based on the projection error of the POD representation. This is an extension of what proposed in a one-dimensional setting in [8]. Let $\mathscr{P}_n$ be the set of points $P_1, \cdots, P_n$ in the parameter space corresponding to actual high-fidelity simulations and $\mathscr{T}_n$ the corresponding Delaunay triangulation. For given number M of POD modes (the size of the basis) we build a set of POD basis functions ϕ_i, $i = 1, \cdots, M$ using the high-fidelity simulations corresponding to points $P_1, \cdots, P_n$. Then we determine the representation error $E(P_k)$, $k = 1, \cdots, n$, corresponding to the residual in the L^2 norm of the projection of high fidelity solutions at P_k on ϕ_i, $i = 1, \cdots, M$. Let us denote $V(T_s)$ the set of vertexes of $T_s \in \mathscr{T}_n$. We select the triangle $T_{\max} \in \mathscr{T}_n$ for which the product of its area and the sum of $E(P_k)$, $P_k \in V(T_s)$, is maximum. The next point of the triangulation is the barycenter of $T_{\max}$.

As an example consider Fig.1. The parameter space $S = [\alpha_0^1, \alpha_0^2] \times [f^1, f^2]$ is mapped to the unit square ($\alpha_0 = [\alpha_0^1, \alpha_0^2] \mapsto \overline{A} = [0,1]$ and $f = [f^1, f^2] \mapsto \overline{F} = [0,1]$) and is partitioned in 8 triangles relative to 7 simulation points that were obtained by iterating the method starting from points P_1, P_2, P_3, P_4. Both Delaunay triangulation (red) and Voronoi tesselation (blue) are presented. The new high-fidelity simulation point P_8 is added at the barycenter of the triangle relative to points P_2, P_4, P_5. For this triangle the product of the area times the sum of the representation errors at the vertexes is the highest.

The procedure implies the computation of n space correlations of high-fidelity solutions for each new simulation point P_{n+1}. These operations are particularly efficient in the hybrid domain-decomposition ROM as the spatial extension of the snapshots and of the POD modes is reduced to a region close to the airfoil. The same procedure can be extended to higher-dimensional parameter spaces.

2.1 Results

We start with a POD basis, called $B_{Initial}$, computed from snapshots taken at 4 points P_1, P_2, P_3 and P_4 (see Fig. 2). 20 time snapshots are uniformly taken over one period for each point P_i, $1 \leq i \leq 4$. Starting from these points in parameter space, 4 additional points, denoted by P_5, P_6, P_7 and P_8 are determined using the method described above (Voronoi tassellation). A suboptimal POD basis, called B_{Subopt} is then computed from these 8 points: P_1 to P_8. We ant to compare the suboptimal basis performance to another basis composed with the same number of sampling points,

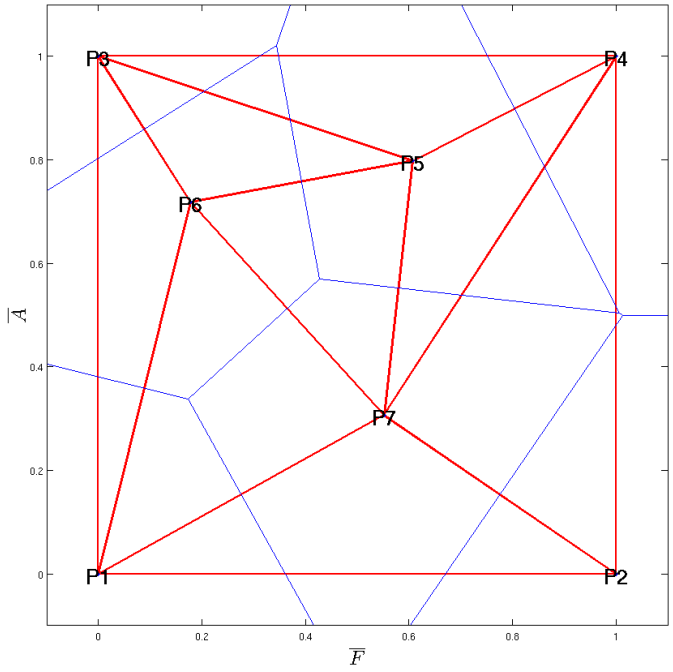

(a)

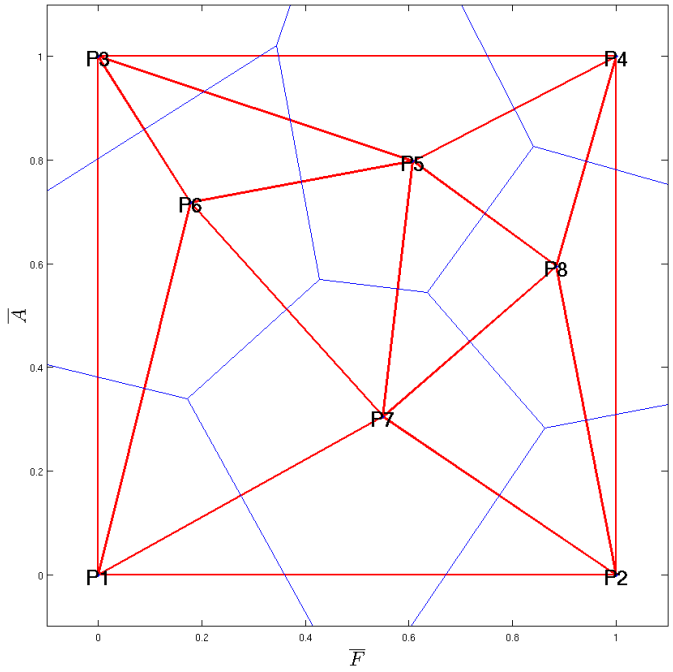

(b)

Fig. 1: Example of one iteration of the Voronoi tessellation algorithm. The parameter space subset S is represented. α_0 is on the ordinates and f on the abscissa. (a) typical iteration (iteration 3); (b) next point is added (P8) and the triangulation updated.

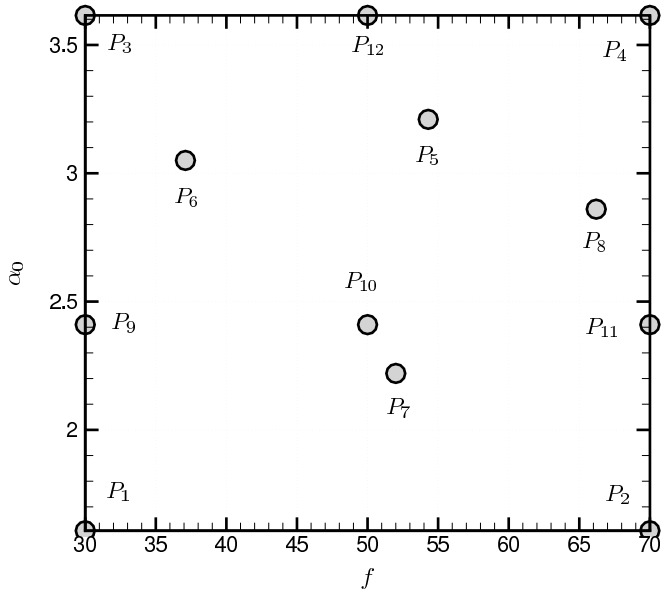

Fig. 2: Sampling of the parameter space.

but chosen arbitrarily. We thus consider an uniform like basis, $B_{Uniform}$, computed from P_1 to P_4 and P_9 to P_{12}. The points P_9 to P_{12} are relative to already existing simulations. A summary of the high-fidelity simulation employed for each POD basis is represented in table 1.

POD basis	P_1	P_2	P_3	P_4	P_5	P_6	P_7	P_8	P_9	P_{10}	P_{11}	P_{12}
$B_{Initial}$ uniform	X	X	X	X								
$B_{Uniform}$ uniform	X	X	X	X					X	X	X	X
B_{Subopt} suboptimal	X	X	X	X	X	X	X	X				

Table 1: POD basis summary.

The accuracy of the 3 POD basis is evaluated by computing the L^2 projection error of the whole snapshot set P_1 to P_{12} onto each POD basis, see table 2. The error P_T denotes the average error evaluated over the whole set of points P_1 to P_{12}. The basis B_{Subopt} shows the best average errors of about 15% compared to $B_{Uniform}$. Even for the extra uniform sampling points P_9 to P_{12} that are not included in the B_{Subopt} database, the errors obtained with B_{Subopt} are close to those obtained with $B_{Uniform}$.

E	P_1	P_2	P_3	P_4	P_9	P_{10}	P_{11}	P_{12}	P_5	P_6	P_7	P_8	P_T
$B_{Initial}$	3.71	3.75	7.36	4.80	6.20	5.25	5.58	3.80	4.69	4.53	3.75	4.63	4.82
$B_{Uniform}$	3.85	4.07	6.70	5.29	4.91	4.20	4.87	4.18	4.38	4.29	3.89	4.45	4.60
B_{Subopt}	3.24	3.23	5.42	5.41	5.11	4.62	4.99	4.20	3.74	3.37	3.01	3.06	4.08

Table 2: POD Basis L^2 projection errors $\times 10^4$. P_T denotes the average error over the 12 points P_i. $B_{Uniform}$ and B_{Subopt} are computed with 160 snapshots. $B_{Initial}$ is computed with 80 snapshots.

3 ROM by domain decomposition

Let $\Omega_a(t)$ denote the two-dimensional region enclosed by the airfoil at time t and let Ω be such that $\Omega_a(t) \subset \Omega \subset \mathbb{R}^2$. The compressible Euler equations are defined on the domain $\Omega_c(t) := \Omega \backslash \Omega_a(t)$. Let us also define two rectangles $\mathscr{R}_e$ and $\mathscr{R}_i$ such that $\Omega_a(t) \subset \mathscr{R}_i \subset \mathscr{R}_e \subset \Omega$. The inner rectangle $\mathscr{R}_i$ always includes the airfoil during its oscillation about a point of the chord.

In $\Omega_c(t)$, we solve the unsteady compressible Euler equations on a fixed cartesian mesh to second order accuracy in space and time, as explained in [6]. We collect an appropriate solution database of N flow snapshots.

Let $U^{(k)}$ be one solution snapshot in $\Omega_c(t_k)$, $1 \leq k \leq N$, restricted to $\mathscr{R}_e \backslash \mathscr{R}_i$ and defined in terms of primitive flow variables. We compute a Galerkin base of the form $\phi_i = \sum_{k=1}^{N} b_{ik}(U^{(k)} - \overline{U})$, with $1 \leq i \leq M$, $\overline{U} = 1/N \sum_{k=1}^{N} U^{(k)}$ and where the coefficients b_{ik} are found as in [10]. This decomposition is performed individually for each primitive variable, i.e. the flow velocity, the pressure and the speed of sound. Consequently each expansion gives an optimal representation of the original dataset.

Let us define $\widehat{U} = \overline{U} + \sum_{i=1}^{M} a_i \phi_i$. The number of global global modes M is very small compared to the size of the computational grid in $\Omega_c(t)$.

The hybrid computational model is obtained by coupling the cartesian grid solver in $\mathscr{R}_e \backslash \Omega_a(t)$ and the Galerkin representation defined in $\mathscr{R}_e \backslash \mathscr{R}_i$. To this end, we follow the steps below:

1. integrate the governing equations in $\mathscr{R}_e \backslash \Omega_a(t)$ by the cartesian solver, with given initial conditions $U^{(n)}$ in $\mathscr{R}_e \backslash \Omega_a(t)$ and boundary conditions on $\partial \mathscr{R}_e$;
2. project the restriction to $\mathscr{R}_e \backslash \mathscr{R}_i$ of the updated solution $U^{(n+1)}$ on the subspace spanned by the POD modes ϕ_i and hence determine $\widehat{U}^{(n+1)}$;
3. recover the boundary conditions to be imposed at the next time step on $\partial \mathscr{R}_e$ as the trace of $\widehat{U}^{(n+1)}$ on $\partial \mathscr{R}_e$;
4. goto (1) until convergence is attained.

This algorithm is fully detailed in [3] for several idealized internal flows. The ratio between the computational cost to solve this hybrid scheme and the cost to solve the flow on the full domain is of the order of the ratio between the area of $\mathscr{R}_e \backslash \Omega_a(t)$ and that of $\Omega_c(t)$.

3.1 Oscillating airfoil in transonic flow

We consider a two-dimensional flow past an oscillating NACA0012 airfoil. The airfoil oscillates about a point fixed at 25% of its chord according to a sinusoidal law. The average angle of attack is 2.89, the amplitude of the angular excursion is 2.41 and the frequency of oscillation is of 50Hz. The Mach number at infinity is 0.6.

The computational domain is $\Omega = 30c \times 20c$, where c is the chord, and the profile is positioned so that the computational domain extends for $10c$ upwards and downwards, $10c$ upwind and $20c$ downwind. The computational grid is $(4.8 \times 10^3)^2$. The simulation has been carried out starting from a uniform initial condition corresponding to the unperturbed flow. Time integration is pursued until the hysteresis cycle is periodic, i.e., after about two cycles of oscillation.

We present in Fig. 3 typical snapshots of the Mach field where the coalescence of the characteristics forms a transient shock on the suction side of the airfoil. The hysteresis cycle is shown in Fig. 4 where the computational results are contrasted to the experimental ones. The computational results are in good agreement with experimental data reported in AGARD R-702.

A collection of 65 snapshots of the flow primitive variables is taken over one period of oscillation once the flow is completely established. The size of the rectangle including the oscillating airfoil $\mathscr{R}_i$ is $1.15c \times 0.2c$, that of $\mathscr{R}_e$ is $2.5c \times 1.0c$.The ratio between the grid points of the full computational domain and those of the hybrid ROM is approximately 260. This ratio corresponds to the CPU time reduction observed between the full computation and the hybrid ROM.

The eigenvalues of the snapshot correlation matrix are shown in Fig. 5. The first four eigenvalues account for about 99% of the database energy for each of the quantities considered. In Fig. 6 the first four POD modes for pressure and vertical velocity are shown. The third and fourth mode, whose energetic contribution is of less than 1% on average, show higher spatial frequencies.

In Fig. 7 we present the normal force coefficient of the actual hybrid simulation for the CT1 test case at 50Hz and at 70Hz. The 50Hz case corresponds to the snapshots used to build the POD modes. Therefore, this test case is designed to check to what extent the hybrid ROM is able to recover the original solution in the optimal situation. In Fig. 7a we show the comparison between the hysteresis curves obtained via the hybrid ROM and that relative to the full computation. The match is perfect. This means that the non-local boundary condition on $\partial\mathscr{R}_e$ (that corresponds to the trace projection operator) is indeed a very good approximation of the transmission conditions between $\partial\mathscr{R}_e$ and $\partial\Omega_c(t)$.

However, the most promising result is that for 70Hz shown in Fig. 7b. Here the hybrid ROM solution, with a boundary operator derived for the 50Hz case, is contrasted to the full simulation at 70Hz. The hybrid ROM starts from an arbitrary initial condition and after a short transient matches almost perfectly the full computation at 70Hz. This case represents a remarkable situation where the ROM leads to a reliable prediction for a case which was not previously included in the database used to build the POD modes.

In Fig. 8 the time history of the coefficients of the pressure modes are depicted. The coefficients pertinent to the Full Order Model are obtained by projecting the snapshots on the POD basis. The coefficients of the hybrid model are those obtained by the above method. An excellent match can be noticed for the first mode, both for 50Hz and 70Hz. For the higher modes still the comparision is very good but slight differences in amplitudes are present. Consequently the presented method is capable to determine the optimal coefficients also for cases which are not included in the database. The error in the force coefficent hysterisis may be decreased by using a more represntative database.

3.2 Discussion

The hybrid ROM implementation here described has limited impact on existing full CFD codes: it is easy to implement since it reduces to a non-local boundary condition. The only addition operation to perform is a projection of the interior domain iterative solution in the space spanned by the POD modes. The validation results that we present show that this method is accurate also for flow conditions that were not included in the database used to build the POD modes.

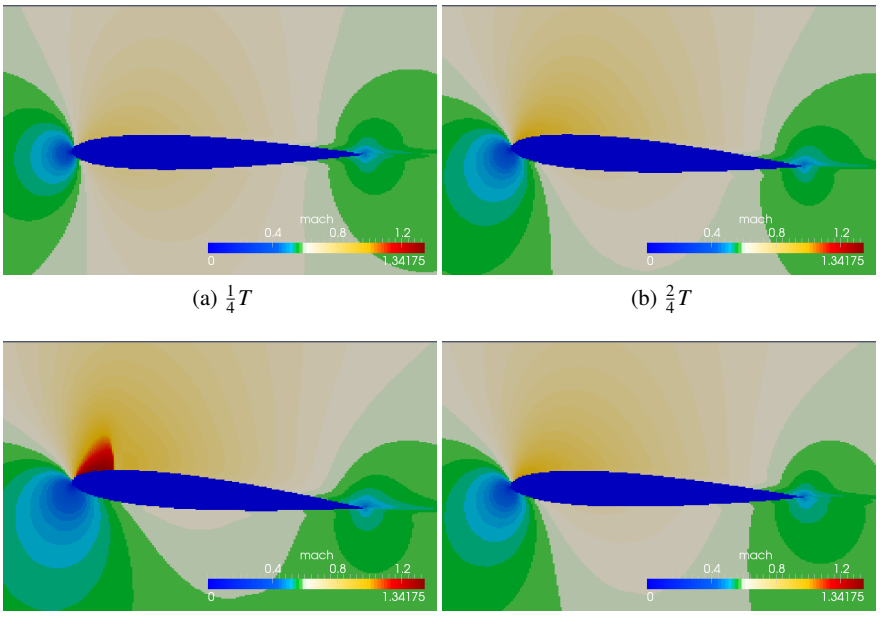

(a) $\frac{1}{4}T$ (b) $\frac{2}{4}T$

(c) $\frac{3}{4}T$ (d) $\frac{4}{4}T$

Fig. 3: Typical Mach number snapshots.

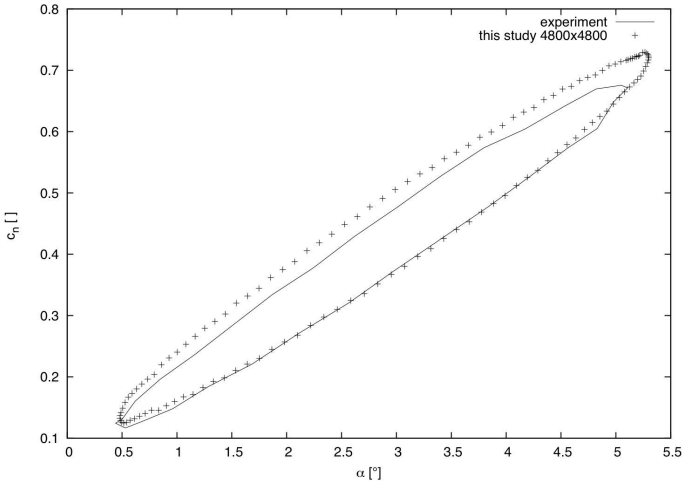

Fig. 4: Normal force coefficient vs. angle. Full cartesian simulation and experimental results from AGARD R702.

4 ROM by optimal transport

Here we describe a non-linear interpolation of the snapshots so that the POD modes may more accurately represent solutions for points in the parameter space that were not included in the database from which they where derived. For a complete survey of this field, see [11, 12]. For an efficient method to numerically solve this problem without obstacles see [7] and references therein.

In order to fix ideas, we consider the case of an oscillating airfoil as in the CT1 test case, for given oscillation amplitude ($\alpha_m = 2.5$deg, $\alpha_0 = 4.$deg) but for several oscillation frequencies. For given phase of the oscillation, i.e. for given pitch of the airfoil our plan is to map the solution for $f = 30$Hz into that of $f = 70$Hz. Thanks to this mapping we can determine a non-linear estimate for the solutions at given pitch for $30Hz < f < 70$Hz.

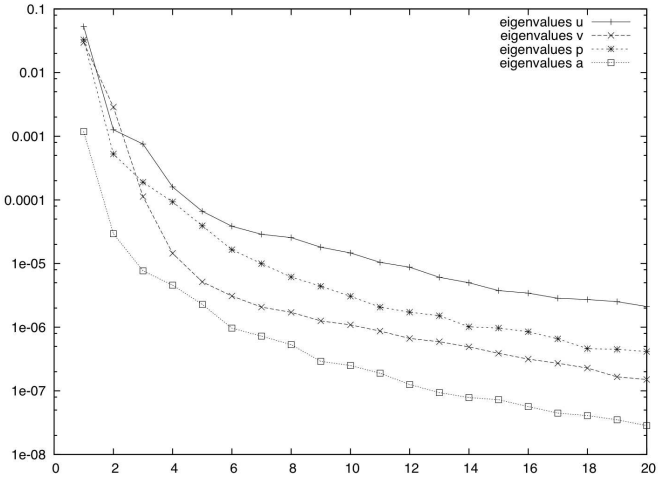

Fig. 5: Eigenvalues of the snapshot correlation matrix for horizontal velocity u, vertical velocity v, pressure p and speed of sound a.

4.1 Transport

In Fig.9 a conceptual description of transport is shown. Given a point $\xi \in \Omega_0$, where $\Omega_0 \subset \mathbb{R}^d$ is a reference configuration, transport at time t is described by a mapping $X(\xi,t)$. The point $x = X(\xi,t)$ belongs to the actual physical configuration $\Omega \subset \mathbb{R}^d$. Let us consider a point x in the actual physical configuration. The inverse mapping, denoted by $Y(x,t)$ (called otherwise backward characteristics), identifies the point in the reference configuration that has been transported by the direct map in x at time t. The following relations hold:

$$\begin{aligned} &x = X(\xi,t), \;\; \xi = Y(x,t), \\ &Y = X^{-1}, \;\; [\nabla_\xi X][\nabla_x Y] = I, \end{aligned} \tag{1}$$

where $[\nabla_\xi X]$ is the jacobian of the transformation $X(\xi,t)$ and $[\nabla_x Y]$ its inverse, i.e., the jacobian of the inverse mapping. Also, we have:

$$\begin{aligned} &\partial_t Y + \mathbf{v} \cdot \nabla_x Y = 0, \;\; Y(x,0) = x \\ &\mathbf{v}(x,t) = \partial_t X, \;\; X(\xi,0) = \xi, \end{aligned} \tag{2}$$

where $\mathbf{v}$ is the velocity field.

Let us consider, as an example, the inviscid Burgers equation:

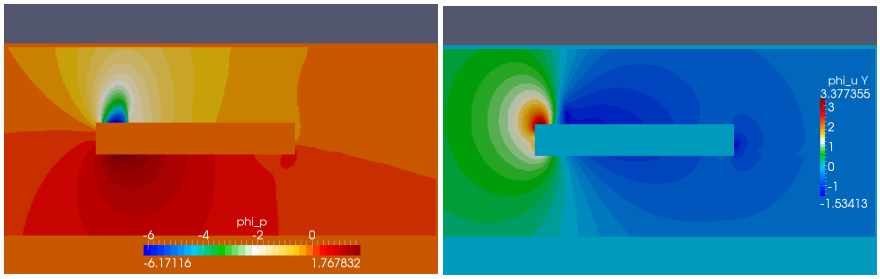

(a) ϕ_1^p

(e) ϕ_1^v

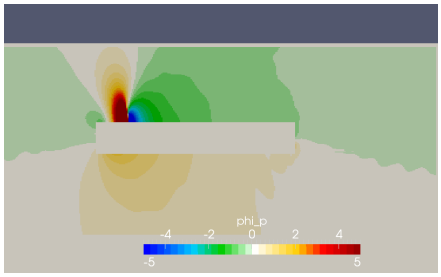

(b) ϕ_2^p

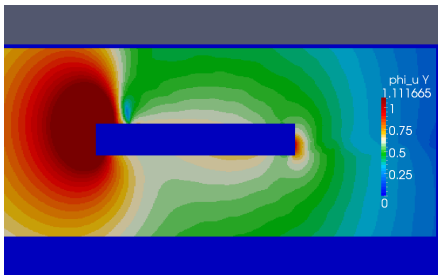

(f) ϕ_2^v

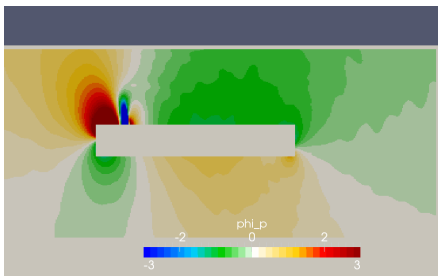

(c) ϕ_3^p

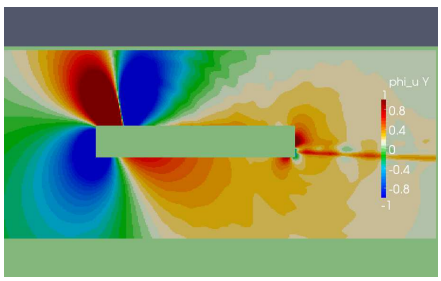

(g) ϕ_3^v

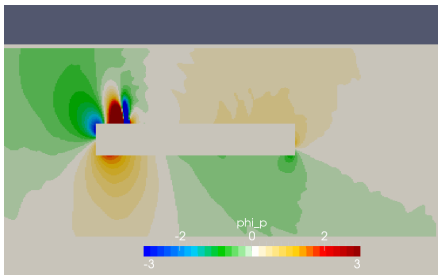

(d) ϕ_4^p

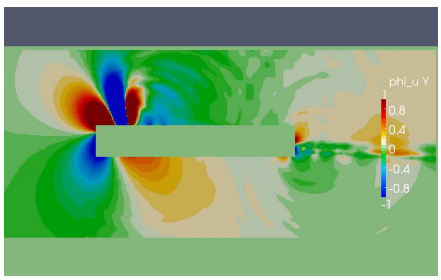

(h) ϕ_4^v

Fig. 6: First four POD modes. Left column pressure, right column vertical velocity

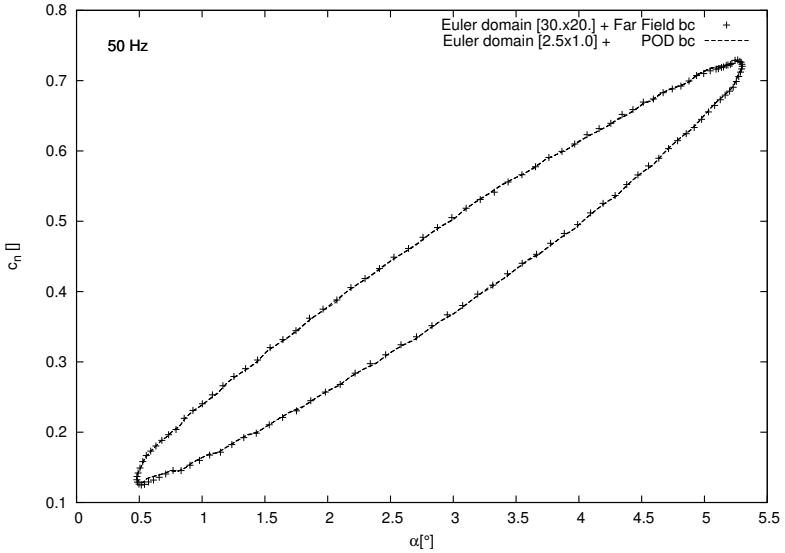

(a) $50Hz$

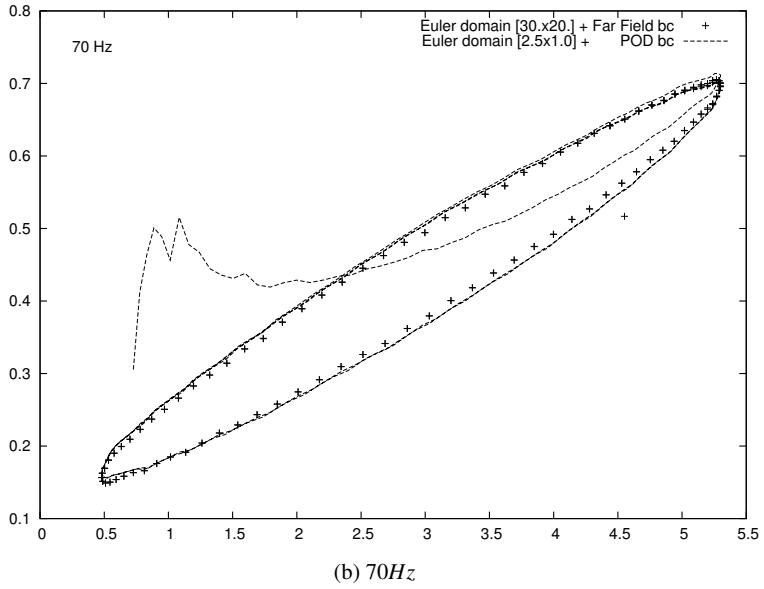

(b) $70Hz$

Fig. 7: CT1 case. Normal force coefficient vs. angle. Full computation vs. hybrid ROM. POD modes are build from the 50Hz simulation only.

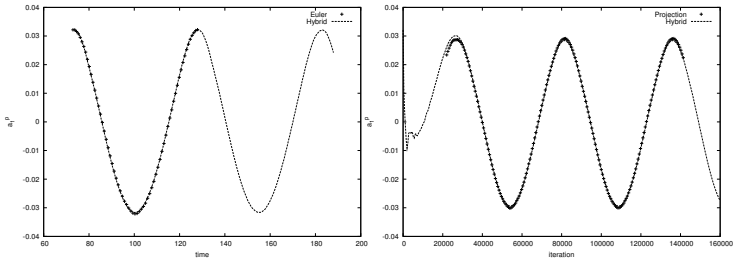

(a) a_1^p

(e) a_1^p

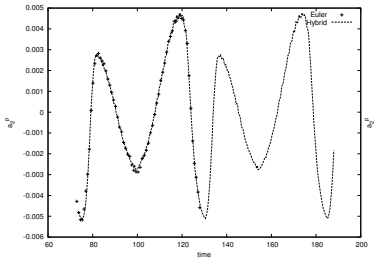

(b) a_2^p

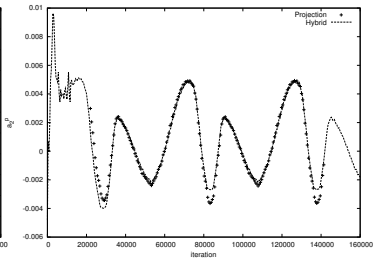

(f) a_2^p

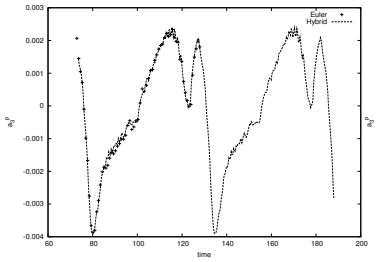

(c) a_3^p

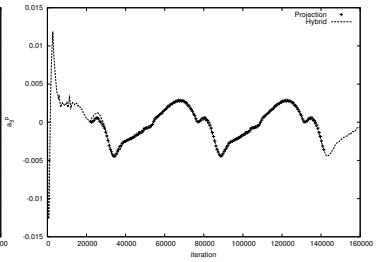

(g) a_3^p

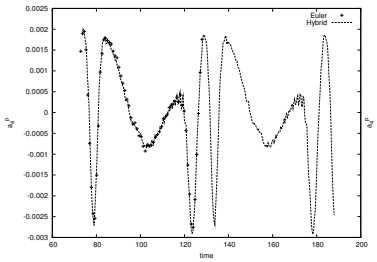

(d) a_4^p

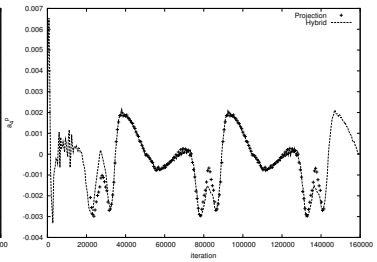

(h) a_4^p

Fig. 8: Coefficients of the first four pressure POD modes. Comparison between full order and hybrid model for 50Hz (left) and 70Hz (right)

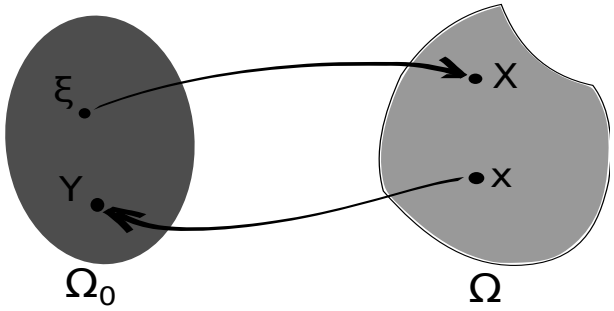

Fig. 9: Lagrangian description of transport: the reference configuration is Ω_0, points $\xi \in \Omega_0$ are transported by the direct mapping in $X(\xi,t)$. Given the actual configuration Ω, a point $x \in \Omega$ is sent back to its counterimage in the reference configuration by backward characteristics, i.e., the inverse mapping $Y(x,t)$.

$$\partial_t \mathbf{v} + \mathbf{v} \cdot \nabla_x \mathbf{v} = 0. \tag{3}$$

This equation describes a pressure-less Euler flow. Since no force is acting on the medium, each component of the velocity field is purely advected. In lagrangian coordinates we have:

$$\partial_t^2 X(\xi,t) = 0 \implies X(\xi,t) = \xi + \mathbf{v}(\xi,0)t. \tag{4}$$

The solution consists of particles moving on straight lines (no acceleration).

In order to determine the mapping, we define a suitable optimal transport problem. Let us associate a scalar density function $\rho(u) \geq 0$ to the solution $u(x,t)$, in such a way that:

$$\int_\Omega \rho(x,t)\, dx = 1,\ \forall t \in \mathbb{R}^+ \tag{5}$$

so that the non-negative density is normalized to 1 for all times. The choice of the density function is for the moment arbitrary. If u is a non-negative scalar and satisfies this normalization, it may be directly used as a density function.

Let ρ_i, $i = 1,2$ be the snapshots of the density function. The optimal transportation problem relative to this density pair is defined as:

$$\begin{aligned} &X^*(\rho_1,\rho_2) = Arg \inf_{\tilde{X}} \left\{ \int_\Omega \rho_1(\xi) |\tilde{X}(\xi) - \xi|^2\, d\xi \right\}, \text{ subject to} \\ &\rho_1(\xi) = \rho_2(\tilde{X}(\xi)) \det(\nabla_\xi \tilde{X}). \end{aligned} \tag{6}$$

The optimal mapping X^* minimizes the cost of the L^2 transport (Monge) problem, among all the changes of coordinates $\tilde{X}(\xi)$ locally keeping constant mass between the densities 1 and 2. The solution to this problem exists and is unique and stipulates that the lagrangian velocity is the gradient of a (almost everywhere) convex potential $\psi(\xi)$.

In particular the same problem can be rewritten in the Eulerian frame of reference. The optimal conditions for the minimum are the familiar conservation law for the density and the previously introduced inviscid Burgers equation. The main difficulty of the problem is that this system is equipped with initial and final condition for the density but no initial condition for velocity. We therefore introduce an approximate Monge mapping as follows:

$$(\rho_1 - \rho_2) = \frac{1}{2}\nabla \cdot ((\rho_1 + \rho_2)\nabla\psi) \tag{7}$$

so that $\nabla\psi = \mathbf{v}(x,0)$ and the inviscid Burgers equation 3 can be used to propagate in time the solution.

4.2 Results

In order to illustrate the method, we have considered the pressure distribution at maximum pitch of the NACA0012 at Mach=0.6 corresponding to a set up similar to the CT1 test case. The densities $\rho_1(x)$ and $\rho_2(x)$ correspond to the pressure distributions in the domain of definition of POD for 30Hz and 70Hz respectively, see Fig.10. In this picture the actual solutions at 30Hz, 50Hz and 70Hz are shown in terms of pressure isolines. It should be remarked that the solution at 50Hz is not a linear interpolation of the solution at 30Hz and 70Hz, see Fig.11. The pressure distribution at 50Hz, see Fig.12, is found thanks to the non-linear interpolation. One-dimensional plots corresponding to a segment in a smooth region and in a region where the shock is present are shown. These results show that the non-linear interpolation method presented here can be used to determine overall reasonable estimates of intermediate snapshots of high-fidelity simulations not present in the database.

5 System identification using ROM in tumor growth modeling

In this section ROMs are applied to system identification in tumor growth modeling. A complete description of the method is presented in [4]. The macroscopic models for tumor growth are represented by a set of PDEs accounting for the phenomenological aspects of the pathology. For the present case, the system reduces to a set of non-linear parametric coupled PDEs that describes the evolution of a three-specie saturated reacting flow in a porous, isotropic, non-uniform medium.

The tumoral tissue is composed by two different phases, denoted by P and Q. The density P represents the number of dividing cells per unit volume, Q is that of the necrotic cells. The healthy tissue is the phase denoted by S. Equations for P, Q and S read:

$$\frac{\partial P}{\partial t} + \nabla \cdot (\mathbf{v}P) = (2\gamma - 1)P, \tag{8}$$

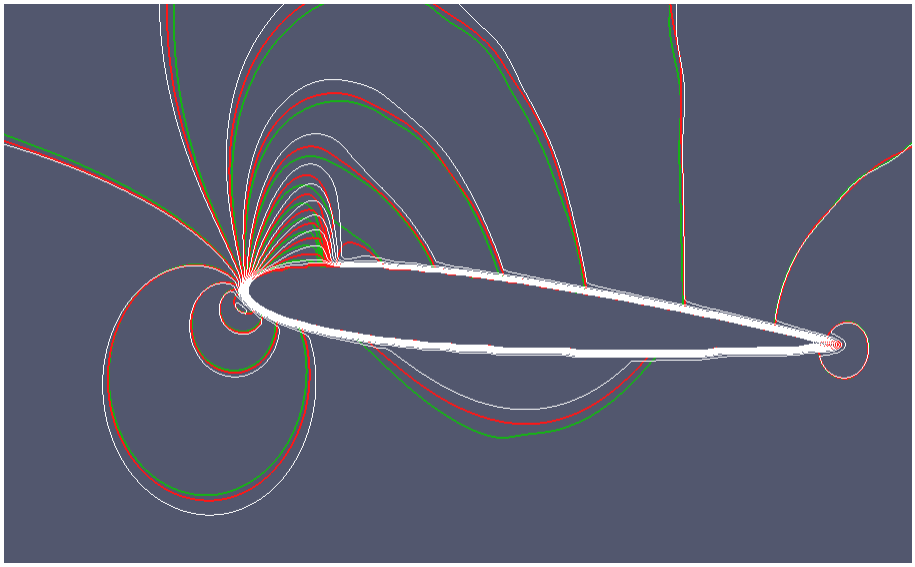

(a)

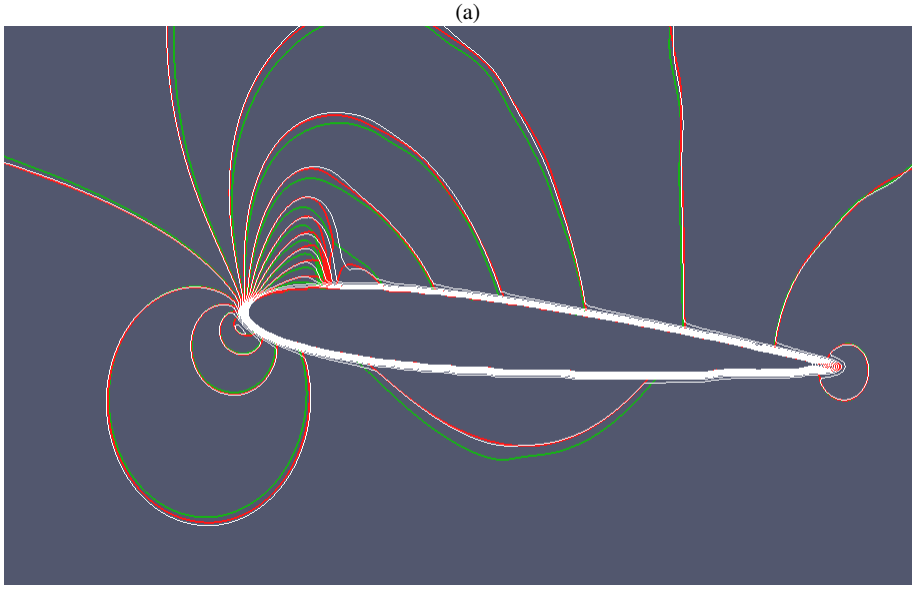

(b)

Fig. 10: (a) Iso-pressure lines of the solution at 30Hz (white), 50Hz (red), 70Hz (green) in the region of definition of POD; the white isolines correspond to the initial condition of the Monge problem. (b) Results of the Monge interpolation: estimated pressure snapshot at 50Hz. Estimated solution in white, actual solution in red. Green: actual solution at 70Hz.

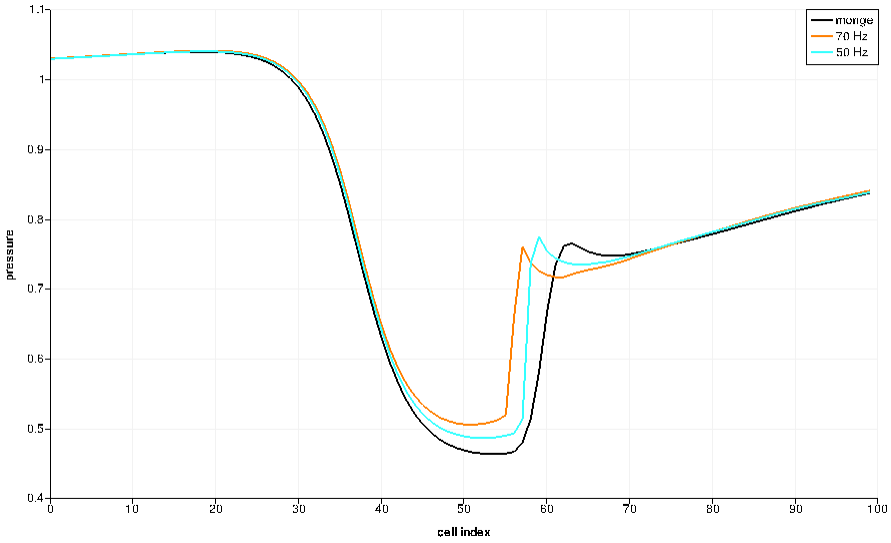

(a)

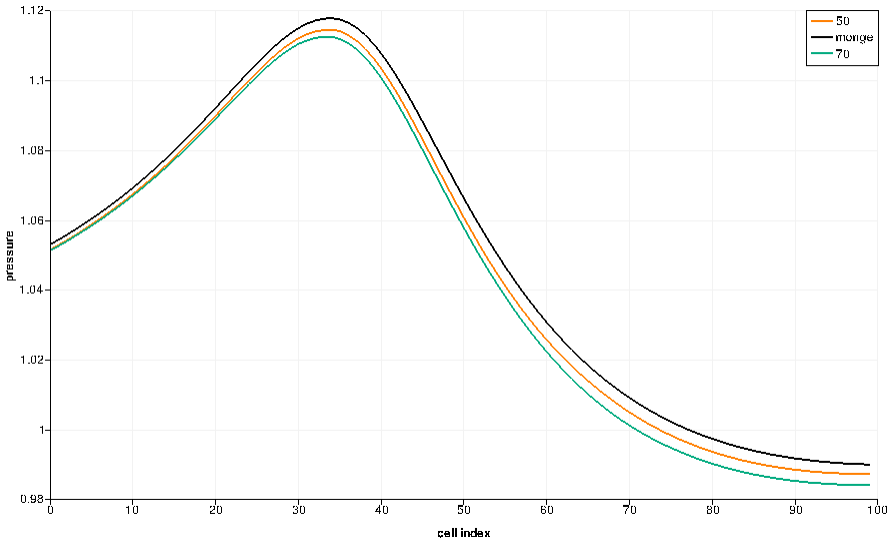

(b)

Fig. 11: Initial condition for the Monge problem (30Hz) and actual high-fidelity solutions (50Hz and 70Hz). (a) curves on a segment parallel to the abscissa where the pressure shows a shock wave; (b) solution on segment where the pressure is regular. The intermediate solution (50Hz) is not a linear interpolation of the initial condition (30Hz) and final condition (70Hz). “Monge” denotes here the initial condition of the Monge problem corresponding to the high-fidelity model at 30Hz.

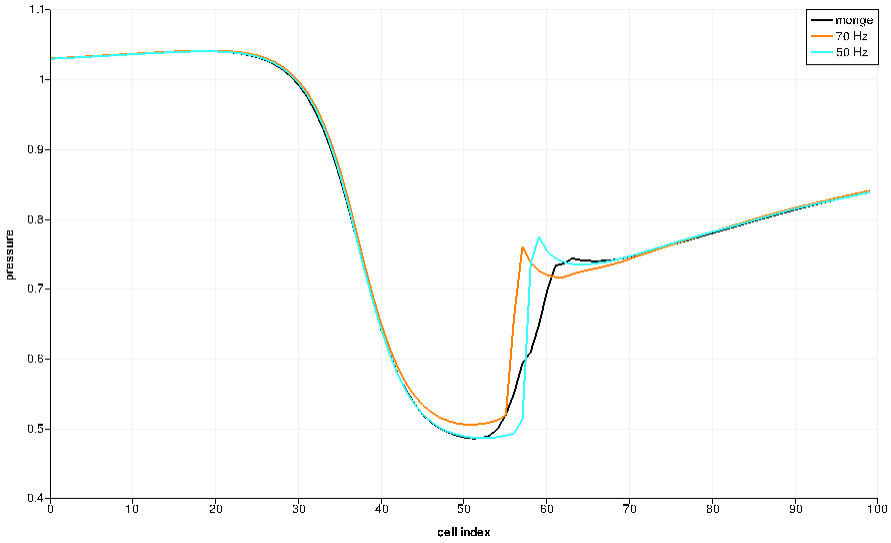

(a)

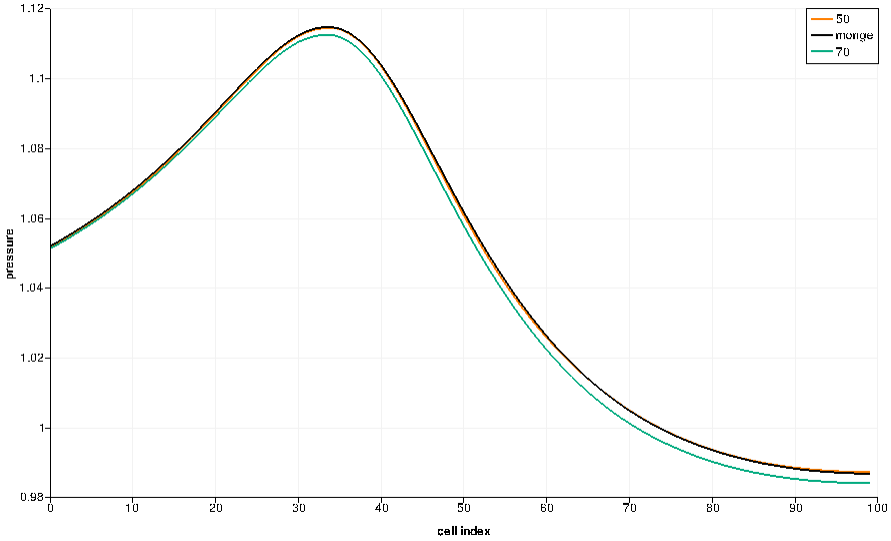

(b)

Fig. 12: Results of the Monge interpolation at 50Hz. The continuity equation and the inviscid Burgers equation are integrated starting from the initial conditions (see Fig.11). The pictures show the high-fidelity model results compared to those of the non-linear interpolation at 50Hz. (a) solution on a segment parallel to the abscissa where the pressure shows a shock wave; (b) solution on segment where the pressure is regular. These are typical results across the field.

$$\frac{\partial Q}{\partial t} + \nabla \cdot (\mathbf{v}Q) = (1-\gamma)P, \tag{9}$$

$$\frac{\partial S}{\partial t} + \nabla \cdot (\mathbf{v}S) = 0. \tag{10}$$

where the velocity $\mathbf{v}$ models the tissue deformation and γ (called the hypoxia threshold) is a scalar function of the nutrient concentration. If enough nutrients are available then $\gamma = 1$ and the tumor cells proliferate, otherwise they die. The healthy tissue evolves through an homogeneous conservation equation.

Assuming that $P+Q+S=1$ in every point of the domain, a condition for the divergence of the velocity field is derived. This condition, coupled with a Darcy law, allows to describe the mechanics of the system:

$$\nabla \cdot \mathbf{v} = \gamma P, \tag{11}$$

$$\mathbf{v} = -k(P,Q)\nabla \Pi. \tag{12}$$

The scalar function Π plays the role of a pressure (or potential), and k is a permeability field, satisfying:

$$k = k_1 + (k_2 - k_1)(P+Q), \tag{13}$$

where k_1 represents the constant porosity of the healthy tissue and k_2 is the porosity of the tumor tissue.

The equation describing the nutrients has the following form:

$$-\nabla \cdot (D(P,Q)\nabla C) = -\alpha PC - \lambda C, \tag{14}$$

where α is the oxygen consumption rate for the proliferating cells, λ is the oxygen consumption coefficient of healthy tissue and $D(P,Q)$ is the diffusivity. Boundary conditions and sources are set up according to the nature of the organs considered and will be detailed later on. The diffusivity may be written as:

$$D = D_{max} - K(P+Q). \tag{15}$$

The link between the nutrients concentration and the population dynamics is provided by:

$$\gamma = \frac{1+\tanh(R(C-C_{hyp}))}{2}, \tag{16}$$

where R is a coefficient and C_{hyp} is called the hypoxia threshold. The resulting hypoxia function thus satisfies $0 \leq \gamma \leq 1$.

For this simple model the state variable set may be defined as $X = \{P,Q,C,\Pi\}$. The observable is defined to be $Y = P+Q$, as result from discussions with medical doctors about what is measured by CT scans in the case of lung metastases. One can not distinguish on images the cell species composing the tumor, but only the tumor mass. The control set consists in all the undetermined scalar parameters describing tissue properties (such as k_1,k_2,D_{max}, K), the tumor activities (nutrient consumptions

α, λ, and C_{hyp}), and the fields describing the initial non-observed conditions needed to integrate the system ($P(x,0)$).

5.1 Regularized inverse problem

The observable evolution is governed by:

$$\dot{Y} + \nabla \cdot (Y\mathbf{v}) = \gamma(C)P. \tag{17}$$

the divergence of the velocity field obeys:

$$\nabla \cdot \mathbf{v} = \gamma(C)P - \frac{\int_\Omega \gamma P \, d\Omega}{\int_\Omega (1-Y) \, d\Omega}(1-Y), \tag{18}$$

where the expression relative to Neumann boundary condition for the pressure field was retained. In the case of Dirichlet boundary conditions the second term of the right hand side of this equation vanishes. The curl of the Darcy law reads:

$$k(Y)\nabla \wedge \mathbf{v} = \nabla k(Y) \wedge \mathbf{v}. \tag{19}$$

and the equation for the oxygen concentration field is written:

$$\nabla \cdot (D(Y)\nabla C) = \alpha PC + \lambda C. \tag{20}$$

The definition of the hypoxia function, γ, is unchanged.

The repeated index summation convention is used from now on. The non-observable variables are expressed as combination of POD modes:

$$\begin{aligned} P &= a_i^P \phi_i^P \quad i = 1,...,N_P; \\ C &= a_i^C \phi_i^C \quad i = 1,...,N_C; \\ \gamma P &= a_i^{\gamma P} \phi_i^{\gamma P} \quad i = 1,...,N_{\gamma P}; \\ \mathbf{v} &= a_i^v \phi_i^v \quad i = 1,...,N_v, \end{aligned} \tag{21}$$

where $a_i^{(\cdot)} = a_i^{(\cdot)}(t)$ are scalar functions of time, $\phi_i^{(\cdot)} = \phi_i^{(\cdot)}(\mathbf{x})$ are functions of spatial coordinates.

The dimension of the empirical functional space, *i.e.*, the number of POD modes used to reconstruct the solution, is chosen such that if additional POD modes are included, the reconstruction of a given field does not vary up to a certain error value that, in this work, was fixed at 10^{-4} in L^2 norm.

Substituting these expressions in the system Eqs. (17) and (20) we obtain:

$$\dot{Y} + a_i^{(v)} \nabla \cdot (Y \phi_i^{(v)}) = a_i^{(\gamma P)} \phi_i^{(\gamma P)}, \tag{22}$$

$$a_i^{(v)}\nabla\cdot\phi_i^{(v)} = a_i^{(\gamma P)}\phi_i^{(\gamma P)} - \frac{\int_\Omega a_i^{(\gamma P)}\phi_i^{(\gamma P)}\,d\Omega}{\int_\Omega 1-Y\,d\Omega}(1-Y), \tag{23}$$

$$a_i^{(v)}k(Y)\nabla\wedge\boldsymbol{\phi}_{\mathbf{i}}^{(v)} = a_i^{v}\nabla k(Y)\wedge\phi_i^{(v)}, \tag{24}$$

$$a_i^{(C)}\nabla\cdot(D(Y)\nabla\phi_i^{(C)}) = \alpha a_j^{(P)}a_i^{(C)}\phi_j^{(P)}\phi_i^{(C)} + \lambda a_i^{(C)}\phi_i^{(C)}, \tag{25}$$

The hypoxia function γ, Eq. (16), is multiplied by P, in such a way that the product γP is:

$$a_i^{(\gamma P)}\phi_i^{(\gamma P)} = a_j^{(P)}\phi_j^{(P)}\frac{1+\tanh(R(a_i^{(C)}\phi_i^{(C)}-C_{hyp}))}{2}. \tag{26}$$

The system Eqs.(22-25) was finally solved by a least square approach under certain constraints that are introduced below. At a given time (say t_0), the snapshot $Y(t_0)$ and a subsequent snapshot $Y(t_1)$ are used to perform the computation of the time derivative. Let the residual of the l-th equation be R_l. We write $F=\sum_l R_l^2$ and

$$\left(a_i^{(\cdot)}(t_0),\pi_j\right) = \text{argmin}\,(F) \tag{27}$$

where $a_i^{(\cdot)}$ are the expansion coefficients for the variables $P,C,\mathbf{v},\gamma P$ and π_j are the parameters to be identified.

The first constraint is linked to the fact that Eq. (25) is an homogeneous equation with respect to the coefficients $a_i^{(C)}$. If $C_{hyp}<0$ the trivial solution is a solution for the whole system Eqs. (22) and (26). In order to prevent the identification of a system with unphysical solutions we get one scalar constraint from the boundary. In the case of Dirichlet boundary conditions $C=C_0$ on $\partial\Omega_C$ where Ω_C is a blood vessel domain, one scalar equation is obtained of the form:

$$\sum_i\left(\frac{\sum_j b_j^i}{\lambda_i^{1/2}}\right)a_i^{(C)}(t)=1,\ \ \forall t. \tag{28}$$

The second constraint to be imposed results from the observation that, since in the inverse problem the equation for the variable P is not solved, the latter does not automatically satisfy: $0\le P\le 1$ and therefore this is a constraint (fundamental for the population dynamics) to be imposed. To this end the residuals are penalized as follows:

$$\tilde{F} = F + c_1(\max\{a_i^{(P)}\phi_i^{(P)}\}-1) + c_2(-\min\{a_i^{(P)}\phi_i^{(P)}\}) \tag{29}$$

where c_1,c_2 are positive constants, set in such a way that penalization does not affect the stability of the procedure (in the present work $(c_1,c_2)\in[1.0,2.5]e-2$).

In order to decrease the computational cost of the procedure a third constraint is imposed to define a feasible set of solutions. The solution is sought so that the admissible values of the POD coefficients belong to an interval I_k that is obtained from I_k^{db}, the corresponding interval in the database, by a stretching factor $1+\delta$ where δ is a suitable positive constant. In all the following simulations the value $\delta=0.1$ was adopted.

The hypothesis that two subsequent snapshots are close in time, or, in other words, that the time between two snapshots is small if it is compared with the characteristic evolution time of the phenomenon, is very optimistic. In order to relax this hypothesis, instead of using first order finite differences, that is equivalent to perform a linear interpolation between the snapshots, a different kind of interpolation is used. However, an higher order finite difference scheme, equivalent to a polynomial interpolation, would require a large number of snapshots. As an alternative, still assuming that only two images are available, an additional hypothesis about the growth rate could be retained. Here, two cases are considered. In the case of exponential growth we write:

$$\dot{Y} \approx Aexp\{\zeta t\} + Bexp\{-\zeta t\} = f(\zeta), \tag{30}$$

where A, B are chosen in such a way that the two available snapshots are interpolated. One parameter, ζ, is free and enters the residual minimization process. The first equation of the system (17-20) becomes:

$$f(\zeta) + \nabla \cdot (a_i^{(v)} \phi_{\mathbf{i}}^{(v)} Y) = a_i^{(\gamma P)} \phi_i^{(\gamma P)}. \tag{31}$$

In the case of a logistic-type growth we proceed in a similar way. We take

$$Y \approx AG(\omega, \sigma) + BG(-\omega, -\sigma) \tag{32}$$

where

$$G(\omega, \sigma) = \frac{\omega e^{\omega t}}{\omega - \sigma e^{\omega t}}. \tag{33}$$

As before A and B are adjusted such that the snapshots are interpolated. In this case, however, we are left with two free parameters (ω and σ) that are found within the residual minimization process. The inverse problem finally takes the form of a nonlinear algebraic optimization problem, that is solved using a Newton trust region method.

5.2 Realistic case application: a comparison with a standard sensitivity approach

In Fig.13 four scans covering an evolution over 45 months are presented of some lung metastases of a primary tumor affecting the thyroid (Courtesy Institut Bergonié). Even though this patient is affected by several metastases, only the study of the one marked in Fig.13.a) will be presented. It is a quasi-steady metastasis, which grows very slowly and thus need only to be monitored. The results obtained by means of a sensitivity technique are presented, when only the first two scans were used in order to identify the system. This means that the first two images were used as data set to solve the inverse problem and find the set of control. Then, the direct simulation

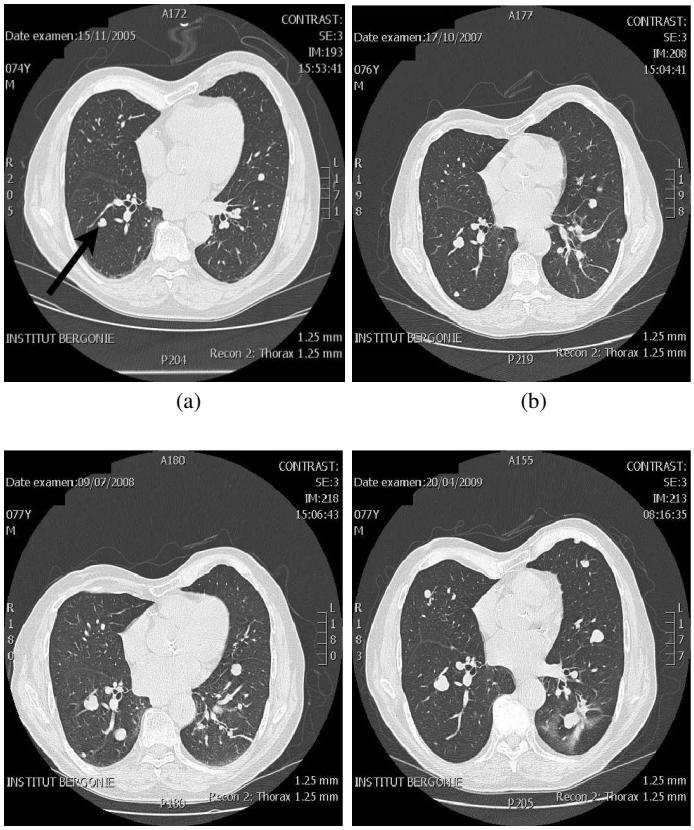

Fig. 13: Scans: a) November 2005, b) October 2007, c) July 2008, d) April 2009

were performed covering the entire evolution and the result has been compared to the data of the subsequent exams.

The control set consists in the parameters and in the initial distribution for the proliferating cell density. In this particular test the initial density distribution for proliferating cells is taken:

$$P(x,0) = A\exp\left\{-\delta\Phi^2\right\}, \tag{34}$$

where Φ is the level set for the tumor, A the amplitude and δ the steepness.

This system is solved at $t = 0$, taking the second image at $t = 0.3$. The time derivative is approximated by a logistic inerpolation. In this particular case it is equivalent to solve the reduced order model for the elliptic equations and to couple them with the residual approximation for the observable. The system is cheap from the computational stand point, its solution taking only few minutes on a standard

laptop. The system was initialized with several initial conditions in order to check the stability and the presence of local minima.

In Table 3 the errors are compared between the sensitivity approach (when two images are taken into account) and the reduced order model. The *ROM* performs quite well in terms of volume in the first part of the growth. For what concerns L^2 norms and in the second part of the growth sensitivity has substantially better results. The most relevant fact is that the two approaches show similar behavior in the very beginning (ROM is solved at $t = 0$). It is interesting that the reduced order model allows to get a correct solution on a time scale that is sufficiently large, *i.e.* on a scale comparable with the interval between two subsequent medical exams. In Fig.14 the

Table 3: Data set and results for realistic case, fitted with the parameters identified by ROM: 6 volumes measures are taken from 2D scans, resolution $1.25mm$.

Month	0	21.0	24.5	36.0	40.5	45.0
Area	4.2e-3	6.5e-3	8.1e-3	9.7e-3	1.03e-3	1.10e-3
$\mathscr{E}_{Sens}(\%)$	0.0	1.8	2.47	2.02	1.94	1.36
$\mathscr{E}_{ROM}(\%)$	0.0	1.9	2.50	2.80	8.67	6.12
$\|Y - Im\|_{Sens}$	0.0	0.22	0.24	0.35	0.31	0.24
$\|Y - Im\|_{ROM}$	0.0	0.23	0.26	0.38	0.36	0.32

fitting curves are shown, confirming essentially what commented about the errors. Let us remark that the two methods starts with exactly the same trend, so that the Reduced Order Model approach results in an approximation of the Sensitivity one in $t = 0$. The Error contours for the third image (*i.e.* the first prediction) are shown for the two methods in Fig.15. On the left, the result of the sensitivity is shown, the reduced order model is on the right. The differences between the two residuals are minimal, showing the ability of the reduced approach to mimic sensitivity.

5.3 A fast rate tumor growth

In order to see if the method is robust enough to perform the identification in a very aggressive case, an exponential fast growth is studied. In Fig.16 the evolution of a metastatic nodule is shown; the evolution takes about six months, the scans are taken at approximately constant rate. The problem is the following one: given the first two scans, we try to recover the third one, after having performed the parameters identification.

A database was build varying all the parameters in uniform intervals. The database consists in 128 simulations. For each one, 20 time frames are taken. The minimization takes about 20 minutes on one standard CPU. In Fig.17.a) the superposition of the simulation to the realistic geometry is shown, at the time corresponding

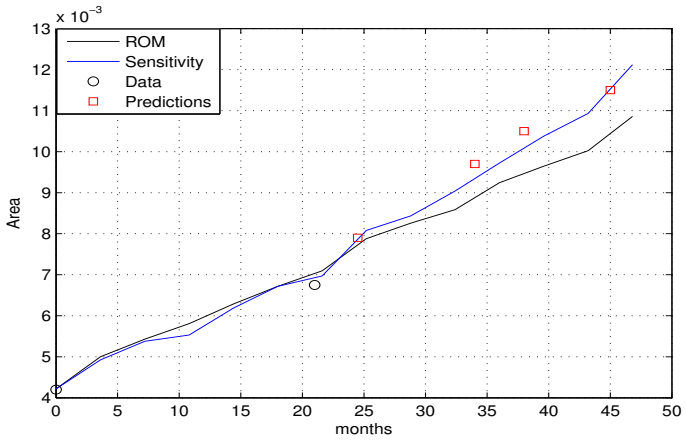

Fig. 14: Area as function of time, for the Reduced Order Model (black line) and for the Sensitivity approach (blue line).

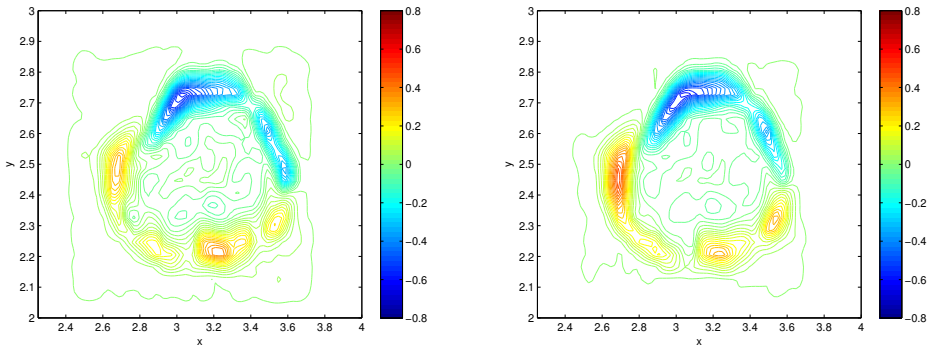

(a) (b)

Fig. 15: Difference between the third scan and the solution when the identification is performed by a) Sensitivity b) ROM

to the third scan. The result is satisfactory, the volume not being too far from the measured one. The error is essentially a shape error. The model tends to regularize the shape, so that the simulated tumor is closer to a spheroid with respect to the real tumor. In order to prevent this error to arise two strategies are possible: the first one consists in modifying the model such that its dynamics is less regularizing and the second one consists in changing the control set.

In Fig.17.b) the volume curve is plotted with respect to days. There is a certain error in volume at the time corresponding to the third scan, but, in terms of time, it is about 15 days on a time interval of 6 months. For such a growth, featured by a

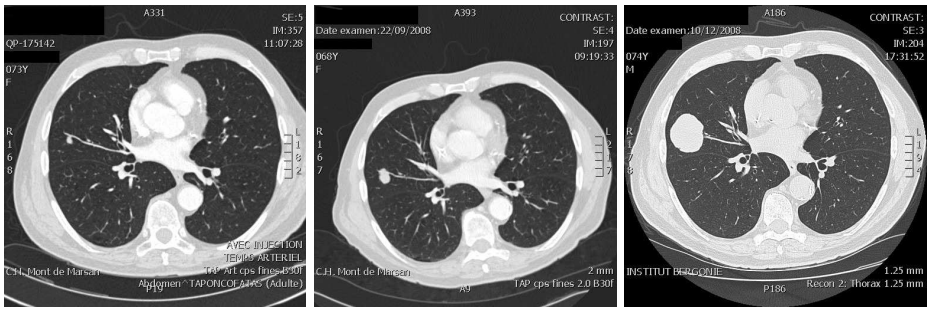

(a) (b)

Fig. 16: Fast growing tumor: scan at a) june 2008 b) september 2008 c) december 2008

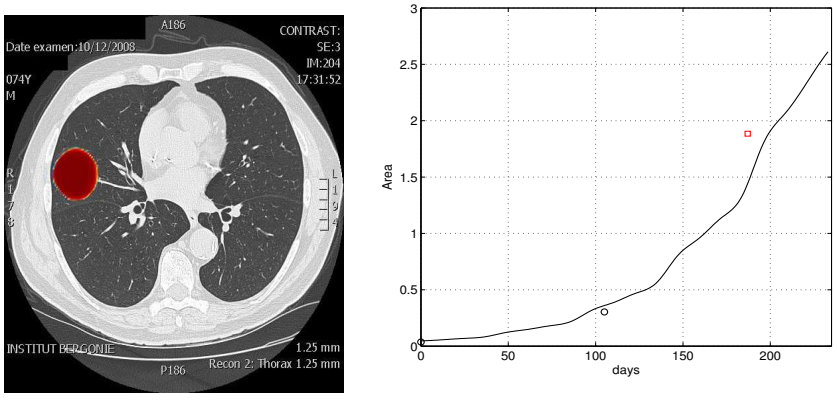

(a) (b)

Fig. 17: Results: a) Superposition of simulation and geometry b) Volume curve with respect to days

high rate and a large final volume, not enough mechanics have been accounted for. As a matter of fact, tumor expansion causes some compression in the tissues and the constraints imposed by the thorax are not negligible.

6 Conclusions

We have presented a set of methods where ROMs have been used to solve problems in applications. ROMs where not directly used for simulation, but instead as an auxiliary numerical expidient in conjunction with full model simulations or availbale data observations. Future investigations will need to improve model accuracy and

robustness with respect to parameter variations, with the objective of accurate and robust predictive ROMs.

Acknowledgements This research is funded in part by the EU FP7 project FFAST, ACP8-GA-2009-233665. We thank Dr. Jean Palussière at the Institut Bergonié, Bordeaux, for selecting the patients and for fruitful modeling discussions.

References

1. M. Bergmann, C.H. Bruneau, and A. Iollo. Enablers for robust pod models. *Journal of Computational Physics*, 228:516–538, 2009.
2. M. Bergmann and A. Iollo. Modeling and simulation of fish-like swimming. *Journal of Computational Physics*, 230:329–348, 2011.
3. M.R. Buffoni, H. Telib, and A. Iollo. Domain decomposition by low-order modelling. *Computers & Fluids*, 38:1160–1167, 2009.
4. Thierry Colin, Angelo Iollo, Damiano Lombardi, and Olivier Saut. System identification in tumor growth modeling using semi-empirical eigenfunctions. *Mathematical Models and Methods in Applied Sciences*, 22(06):1250003–1, 2012.
5. B. Galletti, C. H. Bruneau, L. Zannetti, and A. Iollo. Low-order modelling of laminar flow regimes past a confined square cylinder. *J. Fluid Mech.*, 503:161–170, 2004.
6. Yannick Gorsse, Angelo Iollo, Haysam Telib, and Lisl Weynans. A simple second order cartesian scheme for compressible Euler flows. *Journal of Computational Physics*, 231(23):7780–7794, October 2012.
7. A. Iollo and D. Lombardi. A lagrangian scheme for the solution of the optimal mass transfer problem. *Journal of Computational Physics*, 230:3430–3442, 2011.
8. E. Lombardi, M. Bergmann, S. Camarri, and A. Iollo. Low-order models: Optimal sampling and linearized control strategies. *Journal Europeen des Systemes Automatises*, 45(7-10):575–593, 2011.
9. Holmes P., Lumley J.L., and Berkooz G. *Turbulence, coherent structures, dynamical systems and symmetry*. Cambridge University Press, 1996.
10. L. Sirovich. Turbulence and the dynamics of coherent structures. Parts I,II and III. *Quarterly of Applied Mathematics*, XLV:561–590, 1987.
11. C. Villani. *Topics in optimal transportation*. American Mathematical Society, 1st edition, 2003.
12. C. Villani. *Optimal Transport, old and new*. Springer-Verlag, 1st edition, 2009.
13. J. Weller, E. Lombardi, and A. Iollo. Robust model identification of actuated vortex wakes. *Physica D*, 238:416–427, 2009.